Tunable topologically protected waveguiding in auxetic nonlinear metamaterials

Tunable topologically protected waveguiding in auxetic nonlinear metamaterials

M. Morvaridi,[1] F. Bosia,[1,*] M. Brun,[2,†] V.F. Dal Poggetto,[3,4] A.S. Gliozzi,[1] M. Miniaci,[4] C. Croënne,[4] N.M. Pugno,[3,5] and G. Carta[2]

[1] *Department of Applied Science and Technology, Politecnico di Torino, Corso Duca degli Abruzzi 24, 10129 Torino, Italy*

[2] *Department of Mechanical, Chemical and Materials Engineering, University of Cagliari, Piazza d'Armi, 09123 Cagliari, Italy*

[3] *Laboratory for Bioinspired, Bionic, Nano, Meta Materials and Mechanics, Department of Civil, Environmental and Mechanical Engineering, University of Trento, Trento, 38123, Italy*

[4] *Univ. Lille, CNRS, Centrale Lille, Junia, Univ. Polytechnique Hauts-de-France, UMR 8520 - IEMN - Institut d'Electronique de Microélectronique et de Nanotechnologie, F-59000 Lille, France*

[5] *School of Engineering and Materials Science, Queen Mary University of London, London, E1 4NS, UK*

(Received 1 February 2024; accepted 9 February 2024; published 13 March 2024)

In this paper, we discuss the possibility of achieving tunable topologically protected edge modes through the application of uniaxial prestrain in an auxetic metamaterial. The proposed structure consists of a thin slab with oriented cuts in a hexagonal lattice, where topologically protected band gaps are opened by introducing a controlled variation in selected cut lengths. Numerical simulations demonstrate the existence of topologically protected and scatter-free wave propagation in the structure at the interface between two subdomains with modified cells, in distinct frequency ranges. For the metamaterial considered in this study, this happens only in the presence of auxeticity. In addition, exploiting geometrical nonlinearity, the application of a uniaxial prestrain can be used to close the band gaps or to modify their frequency range, i.e., to weaken the localization effects or to shift the frequency at which they occur. The spatial and temporal variation of the applied strain field can thus be used for the dynamic tuning of metamaterial topological waveguiding properties, with applications in mechanical devices for logic operations and computation.

DOI: 10.1103/PhysRevApplied.21.034024

I. INTRODUCTION

Auxetic materials (i.e., materials with negative Poisson's ratio) exhibit the property of contracting or expanding laterally when they are compressed or stretched longitudinally, respectively [1–4]. This property leads to an unconventional mechanical behavior that can be exploited in various fields, such as biomedical engineering [5–7], energy harvesting [8–11], textiles and sporting goods [12], armours and ballistic protection [13]. More recently, auxetic metamaterials [14,15] have been studied for their enhanced mechanical properties compared to conventional materials, like indentation resistance [16], impact energy absorption [17,18], and fatigue performance [19, 20]. Recent studies have shown that the construction of a hierarchical structure can lead to enhanced auxetic properties [21], including extremely negative Poisson's ratio values (close to the lowest limit of -1 for isotropic media) by activating kirigamilike behavior and exploiting the interaction between scales [22].

So far, most of the investigations on the properties of auxetic materials and metamaterials have focused on their static behavior, but there are indications that many attractive features also appear in their dynamic properties [23–25], including anomalous elastic wave polarization [26] or smart transformation optics [27]. Auxetic metamaterials are thus ideal candidates to explore possibilities in the control of elastic waves, allowing attractive quasistatic and dynamic properties to be combined.

In this context, topological protection has recently emerged as a unique means to propagate waves through sharp corners or bends [28,29], being robust with respect to structural disorder [30,31], line defects [32] or backscattering. Initially introduced in the field of condensed-matter physics [33,34], topological protection has then been largely investigated in classical systems, such as photonics [35], mechanics [36], and elastic waves [37]. Topological elastic metamaterials are analogous to their electronic and optical counterparts, including quantum Hall [38–40], quantum spin Hall [41,42], and quantum valley Hall [43] effects, supporting chiral [44–46], helical [42,47], and valley modes [48–50], respectively. Topologically protected modes arise from the breaking of specific classes

*federico.bosia@polito.it
†mbrun@unica.it

of symmetry in correspondence of a Dirac cone [51] and have been exploited for the design of waveguides with negligible backscattering both in phononics [47,52] and mechanical metamaterials [51,53–56].

Despite the high potential demonstrated so far by topological metamaterials, most of the proposed approaches are based on parametric tunability (e.g., Refs. [57,58]), and lack dynamic tunability, meaning that their operational frequency cannot be changed once the device is designed. To address this issue, dynamically tunable metamaterials [59], whose wave-manipulating properties can be modified by various types of actuations (mechanical stimuli, heat transfer, chemical reaction, and electromagnetic interaction), have been recently proposed. For example, band-gap tunability can be achieved using magnetoactive [60] or photoresponsive [61] materials, wave guiding can be attained in piezoelectric phononic crystals [62], or complex rectifying devices can be realized in acoustics using piezoelectric membranes [63]. The use of programmable switches connecting bonded piezoelectric patches has been exploited for dynamic reconfigurable topological waveguiding [64]. A tunable elastic valley Hall insulator has been designed, exploiting the displacement of a magnetic fluid in a cavity using programmable magnet arrays [65]. Mechanically triggered variations have also been proposed, e.g., the use of prestress to tune wave band gaps [66–68], also realized experimentally. The use of pressure to deform a lattice system and break space-inversion symmetry has been exploited in [69] to create acoustic topological edge states in trusslike hexagonal lattices. However, in continuous media, strains or deformations need to be relatively high to obtain significant changes, with correlated damage risks. One way to address this problem is to use soft materials (e.g., elastomers), with the additional complication of large deformations, nonlinearity, buckling, and instabilities [70–72]. An alternative to this could be to use auxetic metamaterials. This enables large volumetric deformations at relatively low values of stress due to the small bulk modulus, while maintaining the shear modulus significantly large (as is typical of a solid), since the ratio between the bulk and the shear moduli, equal to $(2/3)(1+\nu)/(1-2\nu)$, tends to zero as Poisson's ratio ν tends to the lowest limit of -1 (for an isotropic medium) [73]. An example of an auxetic metamaterial to demonstrate band-gap tunability has recently been presented in [74]. However, this type of mechanical tunability remains to be demonstrated for applications, such as topological waveguiding.

In this paper, we present the design and numerical analysis of an auxetic metamaterial whose topologically protected waveguiding properties can be reversibly tuned by applying external prestrains. The paper is organized as follows. In Sec. II, we discuss the dispersion properties of an auxetic medium with cuts arranged in a hexagonal pattern, for which the opening of band gaps in correspondence of broken Dirac cones is obtained by perturbing the cut lengths. The topological properties of the system are quantitatively demonstrated by calculating the Berry curvature and the valley Chern number. In addition, we perform numerical simulations to show the occurrence of robust wave propagation at the interface between two subdomains, consisting of cells with different perturbations of the cut lengths. In Sec. III, we introduce the effect of a uniform prestrain considering that the material is nonlinear. We show that the presence of an externally applied uniaxial strain can cause the interfacial wave to disappear or be shifted to a different frequency. An additional computation shows the robustness of the proposed effect where, as a consequence of the application of a nonuniform prestrain, wave localization is lost in a finite region, but naturally reappears beyond it, where the prestrain is absent. In Sec. IV, we present some concluding remarks, and in the Appendices, we provide additional details.

II. AUXETIC TOPOLOGICAL METAMATERIAL

A. Unit-cell definition and dispersion properties

Based on previous work [22,75,76], we consider a thin slab with oriented cuts, consisting of hexagonal unit cells that are periodic in the directions defined by the lattice vectors $\mathbf{a}_1 = (1, 0)^{\mathrm{T}}$ and $\mathbf{a}_2 = \left(1/2, \sqrt{3}/2\right)^{\mathrm{T}}$ in the plane x-y, as shown in Fig. 1(a). We start from a unit cell with cuts of equal length, which displays C_6 symmetry [Fig. 1(b)]. The cuts are all rotated by the same relative angle $\theta = \pi/4$ with respect to the cell edges, as shown in Fig. 1(b). To break the C_6 symmetry and open a topological band gap, we modify the hexagonal unit cells by shortening three cuts (II, IV, VI) out of six, to obtain a C_3 symmetry [Fig. 1(c)]. The length of the shorter cuts in the C_3-symmetric unit cell is given by $a + b - 2l'$ [see Fig. 1(c) for the symbols].

The auxetic behavior of both geometries (C_6 symmetric and C_3 symmetric) is evaluated considering a periodic elementary cell and numerically determining the effective Poisson's ratio and Young's modulus by applying macroscopic strains and periodic boundary conditions [22] (the computation is performed in the linear elastic regime and the matrix material is assumed to be isotropic). The hexagonal C_6 and the trigonal C_3 symmetries ensure the in-plane isotropy of the low-frequency effective behavior [77]. The isotropy is also demonstrated by the isofrequency contours reported in Appendix A. For the C_6-symmetric cell, we obtain an effective Poisson's ratio, which is very close to the lower limit for isotropic media of -1, i.e., $\nu_{\mathrm{eff}} = -0.98$. For the C_3-symmetric cell, there is an increase in the effective Poisson's ratio, which, for the parameters considered in this work (see below), is given by $\nu_{\mathrm{eff}} = -0.36$, implying that the material is still auxetic.

We begin by computing the dispersion properties and constructing the band diagrams to describe the in-plane

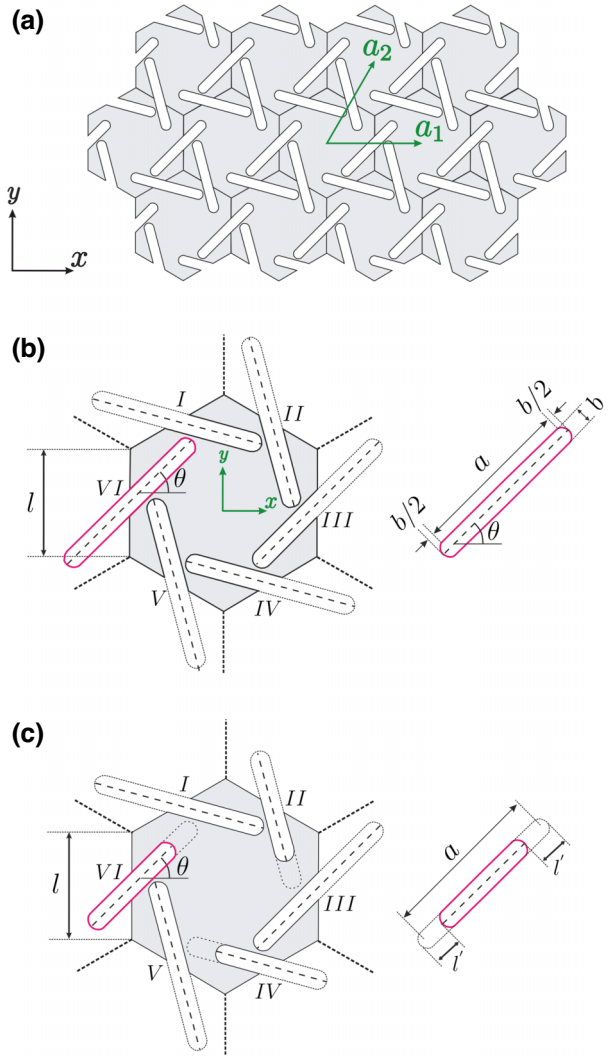

FIG. 1. Schematic representation of the porous metamaterial in C_6-symmetric and C_3-symmetric configurations. (a) The hexagonal lattice composed of the periodic unit cells along lattice vectors $\mathbf{a}_1$ and $\mathbf{a}_2$. (b) The geometrical details of the C_6-symmetric unit cell (all the cuts have the same length $a+b$). (c) The geometrical details of the C_3-symmetric unit cell after C_6-symmetry breaking (the cuts II, IV and VI have length $a+b-2l'$).

wave-propagation behavior of periodic systems obtained by the repetition of the C_6-symmetric and C_3-symmetric unit cells presented in Fig. 1. These relations are computed by enforcing Bloch-Floquet periodic boundary conditions on the edges of the hexagonal unit cell and scanning the contour of the corresponding irreducible Brillouin zone, with high-symmetry points given by $\Gamma \equiv (0,0)$, $K \equiv (4\pi/3L, 0)$, and $M \equiv (\pi/L,\ \pi/L\sqrt{3})$, where $L = \sqrt{3}l$ is the distance between the centers of two adjacent unit cells. The geometrical parameters of the unit cell are taken as follows: cut length $a = 13$ mm, cut width $b = 1.6$ mm, hexagonal cell size $l = 9$ mm, and cut length reduction $l' = 2.5$ mm. The material properties are considered as representative of an elastomeric material with Lamé moduli $\mu = 283$ kPa and $\lambda = 806$ kPa, and specific mass density $\rho = 970\ \mathrm{kg/m^3}$ [78]. Finite-element models are obtained by discretizing the unit cell using second-order triangular and quadrangular plane elements with a characteristic length of 0.25 mm. The corresponding stiffness and mass matrices are obtained considering plane stress behavior.

The band structure of the unit cell with equal cuts [Fig. 2(a)] exhibits two Dirac cones in correspondence with the K point, which represent single contact points between pairs of dispersion surfaces, where two modes become degenerate [56]. The existence of Dirac cones and their dependence on various unit-cell and wave-vector symmetries have been previously described in the literature [79]. Specifically, reducing the C_6 symmetry of the unit cell to a C_3 symmetry type maintains the C_3 symmetry of the wave vector (and thus also the K point), but shifts the degeneracy type of the Dirac cone from deterministic to accidental [80]. In the case of our proposed unit cell, the opening of a total band gap in the vicinity of the broken Dirac cone is observed for the auxetic metamaterial when the C_6 symmetry is reduced to the C_3 type. In Appendix B, we show that this effect does not occur in the corresponding nonauxetic system.

The geometry variation adopted to break the C_6 symmetry, reducing it to C_3 symmetry, and therefore to obtain a topologically protected state in the system, is detailed in Fig. 1(c). For this C_3-symmetric unit cell, band-structure calculations [Fig. 2(b)] confirm that three band gaps appear in the frequency ranges of 265–328, 384–456, and 500–511 Hz. It is interesting to notice that the first and third band gaps are opened between the dispersion branches, which form Dirac cones in the case of the C_6-symmetric unit cell, thus suggesting their topological nature.

B. Determination of the valley Chern number for the C_3-symmetric unit cell

We now study the topological properties of the perturbed structure (C_3-symmetric unit cell), characterized by two types of cuts with different lengths. To ensure that the considered perturbed structure can support topologically protected edge modes, we calculate the valley Chern number and the map of the Berry curvature in the reciprocal space.

For each dispersion surface, we compute the eigenmode displacement $\mathbf{U}(\mathbf{k}) = (U_x(\mathbf{k}),\ U_y(\mathbf{k}))^{\mathrm{T}}$ for different values of the wave vector $\mathbf{k} = (k_x, k_y)^{\mathrm{T}}$ in the reciprocal space. We notice that the frequency of the eigenmode at any value of $\mathbf{k}$ also depends on the choice of the dispersion surface.

The *valley Chern number* is defined as [50,81]

$$C_v = \frac{1}{2\pi}\int_A \Omega(\mathbf{k})\mathrm{d}^2\mathbf{k}, \tag{1}$$

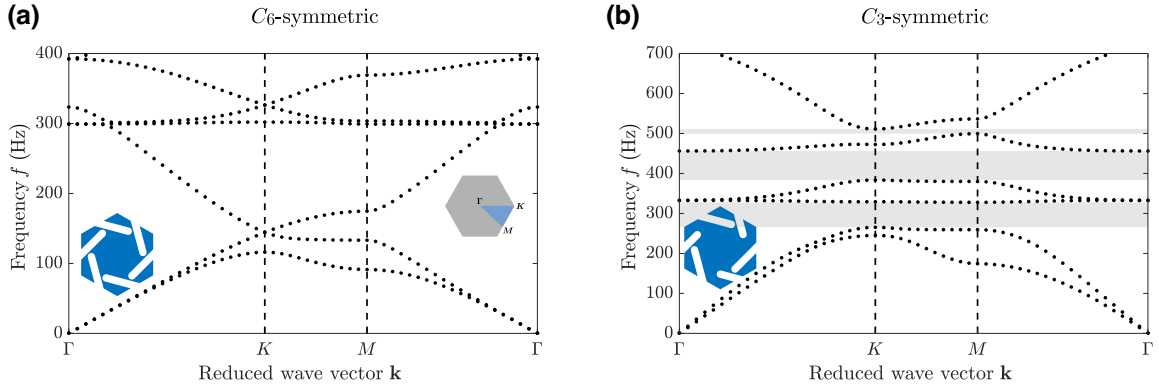

FIG. 2. Band diagrams for the in-plane behavior computed for (a) C_6-symmetric and (b) C_3-symmetric unit cells. Total band gaps are marked in gray. The occurrence of Dirac cones in the case of a C_6-symmetric unit cell (a) is associated with the opening of band gaps in the C_3-symmetric unit cell (b).

where $\Omega(\mathbf{k})$ represents the *Berry curvature* and A denotes a small area around a "valley". In fact, since the considered perturbed system does not break time-reversal symmetry, the integration of the Berry curvature over the whole Brillouin zone is null; nonetheless, the Berry curvature is localized at specific positions ("valleys") of the reciprocal space, in particular around K and K' points (see Fig. 3), so that the integration of $\Omega(\mathbf{k})$ over a small area in correspondence of these points is different from zero.

For each isolated dispersion surface, we calculate the Berry curvature $\Omega(\mathbf{k})$ over a prescribed domain of the reciprocal space bounded by four Γ points (rhombus-shaped Brillouin zone, see Fig. 3) using the following procedure. First, we subdivide the domain into small rhombus-shaped patches, whose vertices are denoted by P_1, P_2, P_3, and P_4 (taken in the counterclockwise direction). For each patch, we compute the $\mathbf{U}(\mathbf{k})$ eigenvectors at the $\mathbf{k}$ values corresponding to the four vertices. Then, we compute the Berry curvature as follows [82]:

$$\Omega(\mathbf{k}) = -\mathrm{Im}\left[\log\left(\frac{\langle \mathbf{U}(P_1)|\mathbf{U}(P_2)\rangle\ \langle \mathbf{U}(P_2)|\mathbf{U}(P_3)\rangle\ \langle \mathbf{U}(P_3)|\mathbf{U}(P_4)\rangle\ \langle\ \mathbf{U}(P_4)|\mathbf{U}(P_1)\rangle}{\langle \mathbf{U}(P_1)|\mathbf{U}(P_1)\rangle\ \langle\ \mathbf{U}(P_2)|\mathbf{U}(P_2)\ \rangle\ \langle \mathbf{U}(P_3)|\mathbf{U}(P_3)\rangle\ \langle \mathbf{U}(P_4)|\mathbf{U}(P_4)\rangle}\right)\right], \tag{2}$$

where

$$\left\langle \mathbf{U}(P_i)|\mathbf{U}(P_j)\right\rangle = \frac{1}{2\pi}\int_S \mathbf{U}^*(\mathbf{k}(P_i))\cdot\mathbf{U}(\mathbf{k}(P_j))\mathrm{d}S. \tag{3}$$

In the formula above, the symbol * indicates the complex conjugate and S represents the area of the periodic cell patch. This procedure is modified in the case of dispersion surfaces that present degeneracies due to their merging (e.g., the first and second dispersion branches degenerate at the Γ point, as do the third and fourth). In this case, it is necessary to compute the Berry curvature for the pair of nth and mth dispersion surfaces using an alternative expression (see Ref. [82]), where all four inner products of the numerator in the previous equation are substituted by the determinant of a 2×2 matrix $\mathbf{P}(P_i,P_j)$ with $P_{11}(P_i,P_j) = \left\langle \mathbf{U}_n(P_i)|\mathbf{U}_n(P_j)\right\rangle$, $P_{12}(P_i,P_j) = \left\langle \mathbf{U}_n(P_i)|\mathbf{U}_m(P_j)\right\rangle$, $P_{21}(P_i,P_j) = \langle \mathbf{U}_m(P_i)|\mathbf{U}_n(P_j)\rangle$, and $P_{22}(P_i,P_j) = \left\langle \mathbf{U}_m(P_i)|\mathbf{U}_m(P_j)\right\rangle$.

The color maps of the Berry curvature associated with the first-second, third-fourth, fifth-sixth dispersion surfaces are shown in Fig. 3. They are computed from the curvatures of the centroids of rhombus-shaped patches of side length $0.005\left(4/\sqrt{3}\right)(\pi/L)$. We note that the Berry curvature exhibits peaks in correspondence of the characteristic points of the reciprocal space, namely K and K', presenting a phase shift between the lower and upper branches for the cases of the first-second and third-fourth bands of the fifth and sixth bands, thus indicating the topological nature of the band gaps between these dispersion surfaces. On the other hand, this phase variation is not observed between the third-fourth and the fifth bands, thus revealing that the band gap, which nucleates in this frequency range, does not present a topological nature.

Using Eq. (1), we can evaluate the valley Chern number at the above-mentioned characteristic points. For all dispersion surfaces, $C_v = 0$ at Γ (vertices of the parallelograms). On the other hand, for the first-second

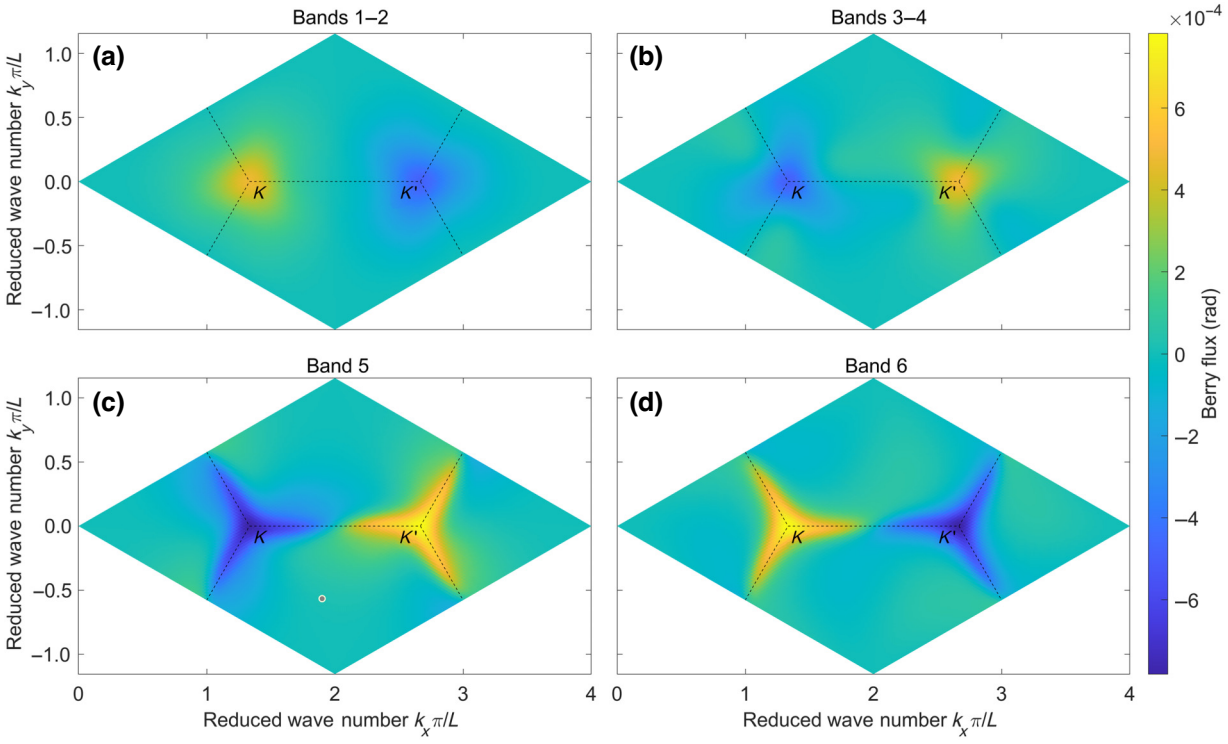

FIG. 3. Values of the Berry curvature Ω in the reciprocal space for the combined (a) first and second, (b) third and fourth, and single (c) fifth and (d) sixth dispersion surfaces of the perturbed structure [C_3-symmetric unit cell, Fig. 1(c)]. The high-symmetry points K and K' are indicated.

and sixth dispersion surfaces, $C_v = -0.49525$ at K while $C_v = +0.49581$ at K'. Opposite values are found for the third-fourth and fifth dispersion surfaces. This confirms that the considered system with broken C_6 symmetry allows the generation of topologically protected edge modes [81].

C. Topological edge modes

The existence of valley edge modes can be verified by considering a supercell consisting of two distinct domains, constituted by the C_3-symmetric unit cells labeled as A (top half) and B (bottom half), comprising a total of 16 unit cells separated by an interface in the middle [Fig. 4(a)]. The number of unit cells is chosen to ensure that a clear spatial separation exists between wave modes occurring at the interface of unit cells with opposing topological phases and their free edges. The unit cell B is obtained by rotating the unit cell A by 60° in the counterclockwise direction. The resulting supercell can be analyzed as a structure, which is periodic in the x direction and has a finite length in the y direction, with free boundary conditions at the top and bottom edges of the supercell. The corresponding dispersion diagram can be computed by scanning the first Brillouin zone, delimited, in this case, by the high-symmetry points $\Gamma(0,0)$ and $X(\pi/L,0)$.

Figure 4 shows the resulting band diagram in three distinct frequency ranges for a clearer visualization, namely 250–330 Hz [Fig. 4(b)], 360–440 Hz [Fig. 4(c)], and 470–550 Hz [Fig. 4(d)]. In each case, the bands that represent localized interface modes are tracked through the modal assurance criterion [83] and highlighted in red. The corresponding wave modes, labeled as I_1 through I_3, are also computed at the X point of the reciprocal lattice and are shown, respectively, inside the green, blue, and orange boxes, with the color bar representing absolute displacement amplitude values. The frequencies of the represented wave modes at the X point are 317, 411, and 525 Hz, respectively, presenting mostly longitudinal polarization (direction of the x axis) along the interface.

D. Propagation of topologically protected modes

The topological waveguiding properties at the interface between the distinct unit cells can be demonstrated by constructing a finite-sized sample with an interface between the unit cell regions A and B determining the preferential direction of ideally scatter-free energy propagation. For this purpose, a finite structure composed of 22×34 unit cells is designed, with a sharp corner of 60° between distinct segments of the interface. This structure, which is commonly used in works dealing with topologically

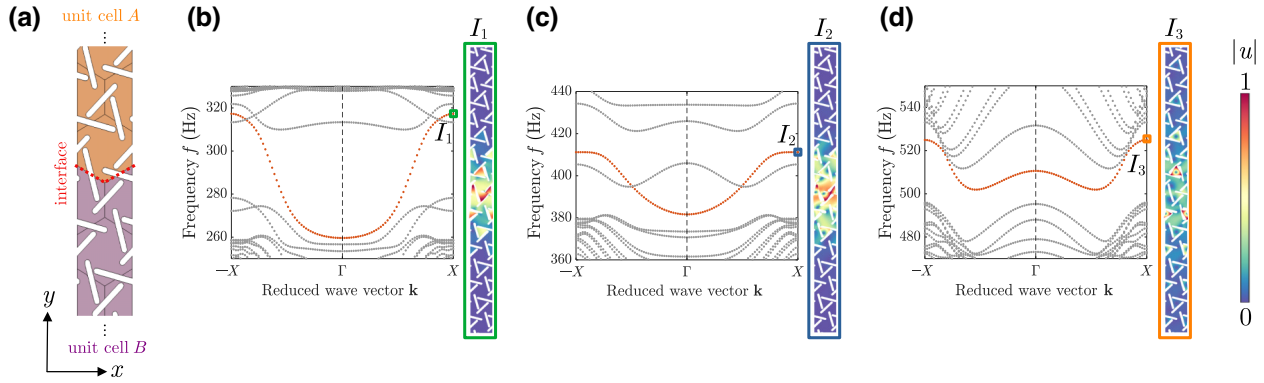

FIG. 4. Band diagrams of the supercell. (a) The supercell is obtained as a finite strip composed of 16 unit cells, with the bottom and top halves constituted by C_3-symmetric unit cells A and B, respectively, rotated by 60° with respect to each other. The resulting band diagrams are shown for distinct frequency ranges, i.e., (b) 250–330 Hz, (c) 360–440 Hz, and (d) 470–550 Hz, with red bands representing topologically localized modes I_1 through I_3, which show most significant relative displacements at the interface of the two subdomains of the supercell. The colorbar represents absolute displacement values ($|u|$).

protected mechanical waveguides [84], is presented in Fig. 5(a), where the interface is highlighted in red and the point where an in-plane excitation is applied is also shown. The direction of the excitation is taken as horizontal, in accordance with the polarization of wave modes $I_1 - I_3$ [Figs. 4(b)–4(d)]. Frequency-domain steady-state analyses are performed considering free-boundary conditions, using signals with single frequencies corresponding to isolated interface modes. The wave mode corresponding to I_1 is excited using a frequency corresponding to the wave number $kL/\pi = 0.65$ (at 295 Hz), thus exciting this isolated wave mode. The second excitation frequency is taken at the X point (at 411 Hz) of the corresponding mode I_2 [Fig. 4(c)]. The results in Figs. 5(b) and 5(c) demonstrate the concentration of energy at the interface between unit cells. In the first case, however, the energy can propagate through the sharp corner due to the topological nature of this band gap. The second excitation frequency leads to energy mostly restricted to the region to the left of the corner, thus revealing that waveguiding cannot be performed efficiently in this case due to the trivial (nontopological) characteristic of this

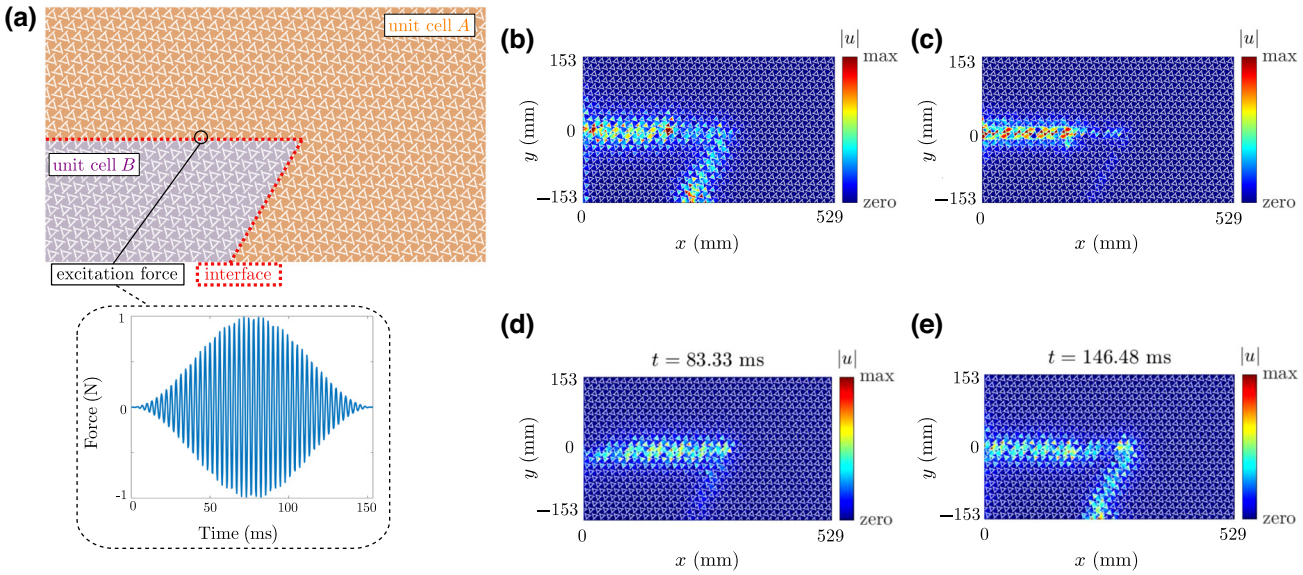

FIG. 5. Topological waveguiding functionality. A finite structure comprised of 22 × 34 unit cells, with the interface highlighted in red, is excited in the horizontal direction at the center of the region indicated by the black circle. The concentration of energy at the interface region is verified by frequency-domain steady-state analyses with input frequencies of (b) 295 Hz and (c) 411 Hz. Transient analysis with applied sine bursts centered at 295 Hz [inset of part (a)] for time instants (d) 83 ms and (e) 146 ms shows excitation of a localized mode, which propagates along the interface.

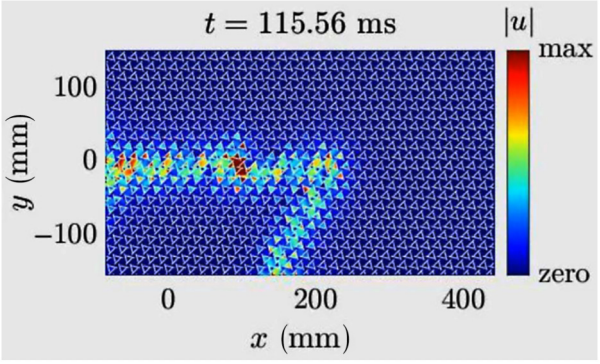

VIDEO 1. Topological waveguiding in a time domain simulation.

band gap. Additionally, a transient analysis is performed using the Newmark method considering a sine "burst" signal obtained by modulating 50 sinusoidal cycles with a Hanning window [inset of Fig. 5(a)] to center the frequency content of the applied input (0.33-ms time-step discretization) around the previously excited I_1 mode. The resulting absolute displacements are shown for distinct time instants in Figs. 5(d) and 5(e), respectively, at 83 ms and 146 ms. The energy is thus shown to be concentrated at the interface between the two unit cell types, with a steep decay moving away from the interface. The presence of the sharp corner does not preclude the propagation of the localized mode and no scattering effects are observed. The propagation in the transient regime is also reported in Video 1.

III. TUNABILITY OF TOPOLOGICALLY PROTECTED WAVE PROPAGATION

A. Band-gap manipulation applying external prestrain

The properties of the discussed auxetic metamaterial can become tunable by applying quasistatically prestrains leading to a nonlinear elastic response. To illustrate this, we choose a Neo-Hookean hyperelastic model [85,86], which describes the reversible nonlinear behavior of materials like polymers or rubbers for large deformations. The hyperelastic strain energy function has the form

$$W(\mathbf{F}) = \frac{\mu}{2}(J_1 - 3) - \mu \ln(J_{\mathrm{el}}) + \frac{\lambda}{2}[\ln(J_{\mathrm{el}})]^2, \quad (4)$$

where $\mathbf{F} = \nabla \mathbf{x}$ is the deformation gradient, with $J_1 = \mathrm{tr}(\mathbf{F}^{\mathbf{T}}\mathbf{F})$ and $J_{\mathrm{el}} = \det(\mathbf{F})$. In the following we will apply a uniaxial stretch $F_{yy} = 1 + \varepsilon_{yy}$ of moderately large amplitude and present results as functions of the strain component ε_{yy}.

Simulations are performed using the structural mechanics and nonlinear elasticity modules of COMSOL Multiphysics. The finite-element analysis is carried out by means of a coupled "stationary" and "eigenfrequency" study, whereby first a large quasistatic prestrain (with values up to 0.2) is applied to the C_3-symmetric unit cell, including material and geometrical nonlinearity, and subsequently the corresponding dispersion surfaces of the deformed unit cells are determined by computing the eigenfrequencies of the deformed cell for each value of the wave vector. We remark that in this case the dispersion surfaces are preferable to the two-dimensional dispersion diagrams, because under prestrain the unit cell deforms and loses its symmetric properties and, hence, dispersion surfaces provide a complete description of the dispersion behavior of the system in the reciprocal plane. Results are presented in Fig. 6 for $\varepsilon_{yy} = 0$, 0.1, 0.2. For nonzero prestrains (parts *b* and *c*), the deformed configurations of the unit cells are also depicted, with the local von Mises-Cauchy stress distribution represented in color scale; for $\varepsilon_{yy} = 0.1$ and $\varepsilon_{yy} = 0.2$, Cauchy stresses reach values of approximately 0.2 and 0.4 MPa, respectively, concentrating at slender material portions at the tip of the cuts, where local deformations are greatest.

The dispersion surfaces of the deformed unit cells of the nonlinear elastic material undergo significant changes compared to those for the unloaded ones. Figures 6(b) and 6(c) show that in the presence of a prestrain of 0.1 and 0.2, respectively, the first topological band gap closes, thus eliminating the possibility of generating topologically protected modes at this frequency, while the second trivial band gap is preserved but shifted to higher frequencies (from 384–456 Hz for $\varepsilon_{yy} = 0$ to 439–485 Hz for $\varepsilon_{yy} = 0.2$). This introduces the possibility of different manipulation of waveguiding effects at the two considered frequency ranges. In the case of the lower frequency range, waveguiding can be eliminated by applying a sufficiently large uniaxial external strain, while in the higher range it can be tuned to higher frequencies. It should be noticed that the effect is mainly due to geometrical nonlinearities, since at the chosen strain levels material nonlinearity has a small influence on results. This has been verified numerically by disregarding material nonlinearity while maintaining geometrical nonlinearity (not shown here for brevity). Results for the dispersion surfaces in this case are very similar to those reported in Figs. 6(b) and 6(c).

In addition, it is worthwhile to underline that the effective Poisson's ratio of the system is not affected significantly by prestrain, as demonstrated in Appendix C.

For a deeper analysis of the phenomenon, a diagram illustrating how the lower two band gaps vary with the externally applied prestrain is calculated. For this purpose, in Fig. 7 we show how the ranges of the band gaps (colored in gray) change with the applied prestrain ε_{yy}. From the figure, it can be seen that the first band gap between $\max(\mathrm{DS}_2)$ and $\min(\mathrm{DS}_3)$ is closed at a strain that is slightly larger than 0.07. Conversely, the second band gap between $\max(\mathrm{DS}_4)$ and $\min(\mathrm{DS}_5)$ is maintained

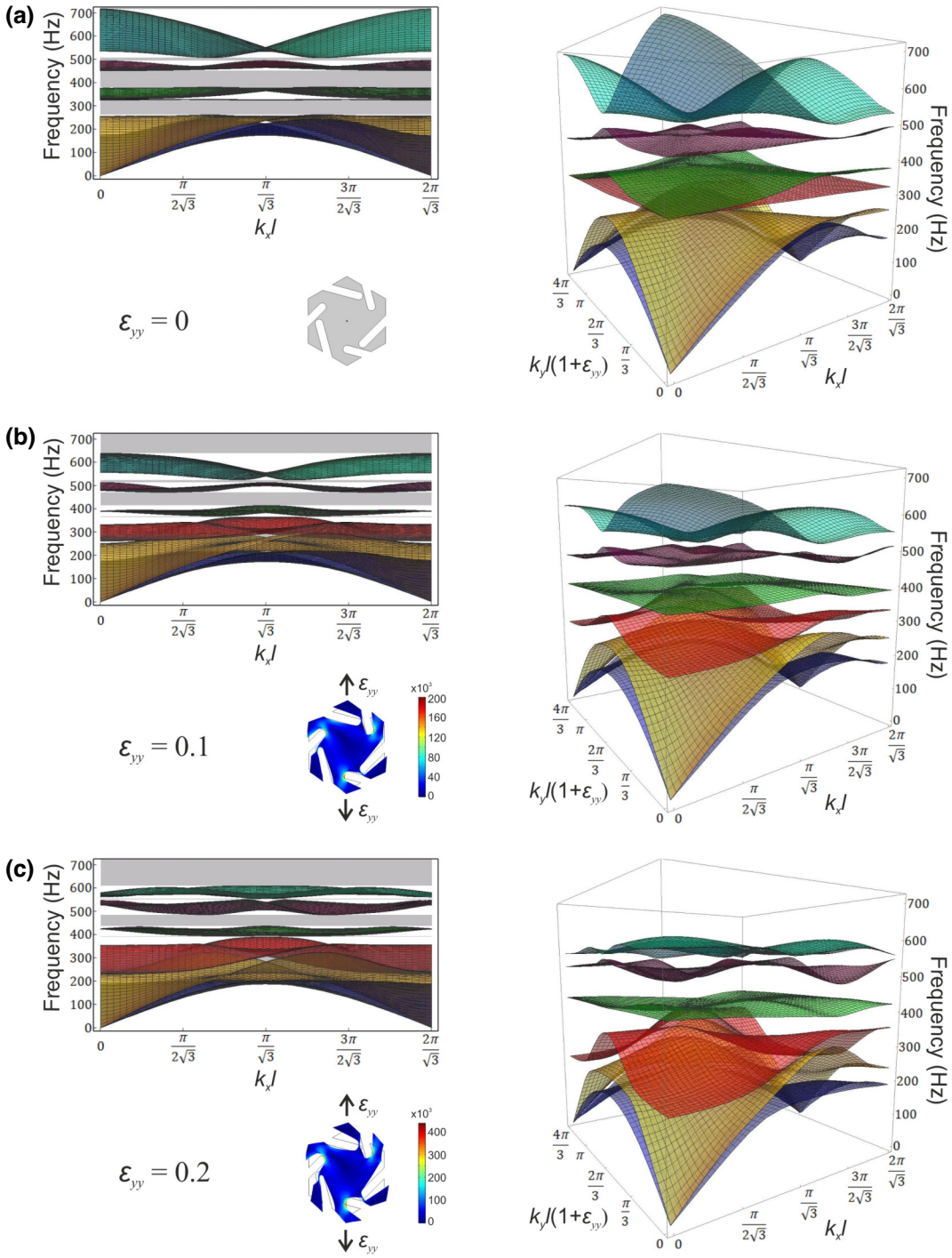

FIG. 6. Dispersion surfaces for (a) $\varepsilon_{yy} = 0$, (b) $\varepsilon_{yy} = 0.1$, (c) $\varepsilon_{yy} = 0.2$, represented in side view (left) and in axonometric view (right); the band gaps are colored in gray in the left diagrams. The deformed configurations of the unit cells are also reported in (b),(c), with von Mises-Cauchy stresses represented in color scale (in Pa).

but shifted to higher frequencies as the value of prestrain is increased; the frequency interval of the second band gap depends on the value of ε_{yy}. Two additional features are retrieved: for nonzero values of prestrain a small band gap between $\max(DS_3)$ and $\min(DS_4)$ appears, whose width remains small as prestrain is increased. Additionally, the band gap at higher frequencies between $\max(DS_5)$ and $\min(DS_6)$ disappears for moderate values of prestrain and reappears again for larger values of prestrain.

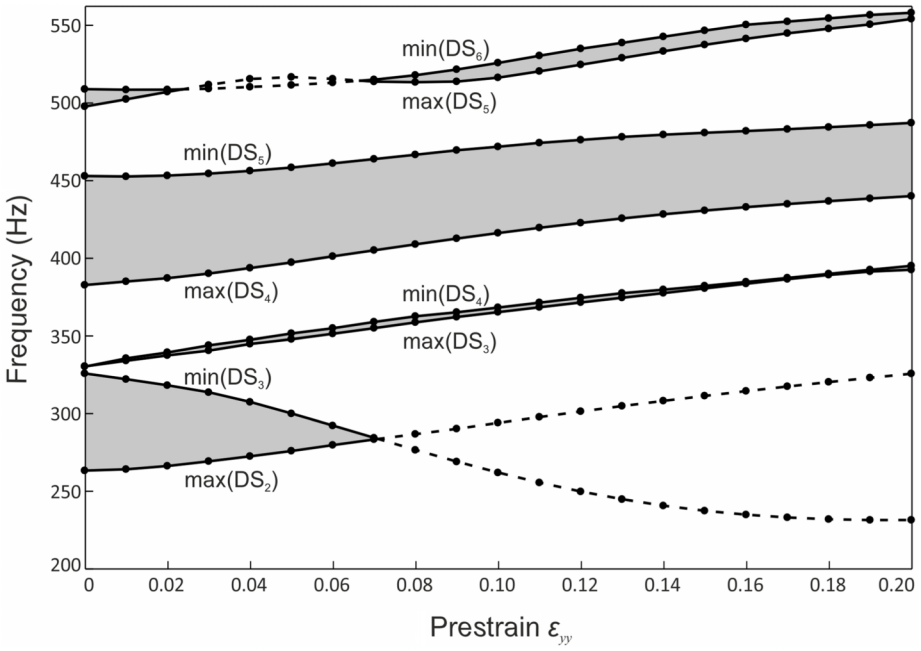

FIG. 7. Frequency ranges of the lower band gaps (in gray color) versus the imposed prestrain ε_{yy}. The band gaps are determined by calculating the minima (min) and maxima (max) of the dispersion surfaces (DS), where the subscript refers to the number of the considered dispersion surface.

B. Tuning waveguiding with external prestrain

To verify the results emerging from band-structure calculations and illustrate how these can be exploited in applications requiring control of waveguiding, we present a configuration, which includes 50 unit cells in the x direction and 32 unit cells in the y direction [Fig. 8(a)]. We perform frequency-domain simulations, exciting signals at the left side of the sample at a fixed frequency of 300 Hz, falling inside the lower topological band gap in the absence of prestrain [Fig. 8(b)] and close to mode I_1 in Fig. 4. We evaluate the propagating wave field for increasing vertically applied quasistatic strain ε_{yy} imposed on the entire upper and lower edges of the specimen. For small strain values [i.e., for $\varepsilon_{yy} \leq 0.05$, Figs. 8(c) and 8(d)], displacements are well localized at the interface between the two domains, as also observed in Fig. 4. With increasing vertical strain, there is a gradual weakening of the localization effect, and a transition to nonlocalized propagation occurs at about $\varepsilon_{yy} = 0.075$ [Fig. 8(e)]. This corresponds to a prestrain value for which the band gap centered at 300 Hz is closed [see Fig. 8(b)]. For $\varepsilon_{yy} = 0.1$ [Fig. 8(f)], no residual localization effects remain. Thus, simulations confirm that the possibility of localized waveguiding is removed when the applied prestrain closes the band gap responsible for the localized mode. As discussed, this is mainly due to the presence of geometrical nonlinearity in the deformation of the auxetic structure.

On the other hand, the application of an external vertical strain can also be exploited to generate a frequency shift in the waveguiding effects of the localized modes at the interface between the two domains. This takes place for wave propagation in the nontopological band gap illustrated in Fig. 9(a). In this case, application of an external vertical prestrain induces a shift of waveguiding effects to higher frequencies: $f = 440$ Hz for $\varepsilon_{yy} = 0.05$ [Fig. 9(b)], 450 Hz for $\varepsilon_{yy} = 0.1$ [Fig. 9(c)], and 462 Hz for $\varepsilon_{yy} = 0.15$ [Fig. 9(d)], respectively. Notice that in this case, the upper and lower band-gap bounds overestimate the range in which interfacial waveguiding occurs, since the localized mode associated with I_2 covers only a relatively small frequency range within the band gap (see Fig. 4). In addition, as expected, the waveguide displays increased backscattering effects at the sharp edge, compared to the topological band-gap case (Fig. 8).

The effect of a quasistatic prestrain field on the localization of waves can also be exploited to modify the waveguiding properties of a structure locally, in a confined region. This is schematically illustrated in Fig. 10 on a specimen composed of 75 unit cells in the x direction and 32 unit cells in the y direction. In this case, we consider a straight waveguide without a sharp angle, since the considered effect is more evident in this type of structure. An external vertical prestrain is applied on a limited length in the centre of the sample (1/3 of the length), as highlighted in Fig. 10(a). In the specific example, waves are excited at 300 Hz, corresponding to the localized waveguiding of mode I_1, and a prestrain value of $\varepsilon_{yy} = 0.1$ is chosen. As shown in Fig. 10(b), the applied prestrain disturbs the

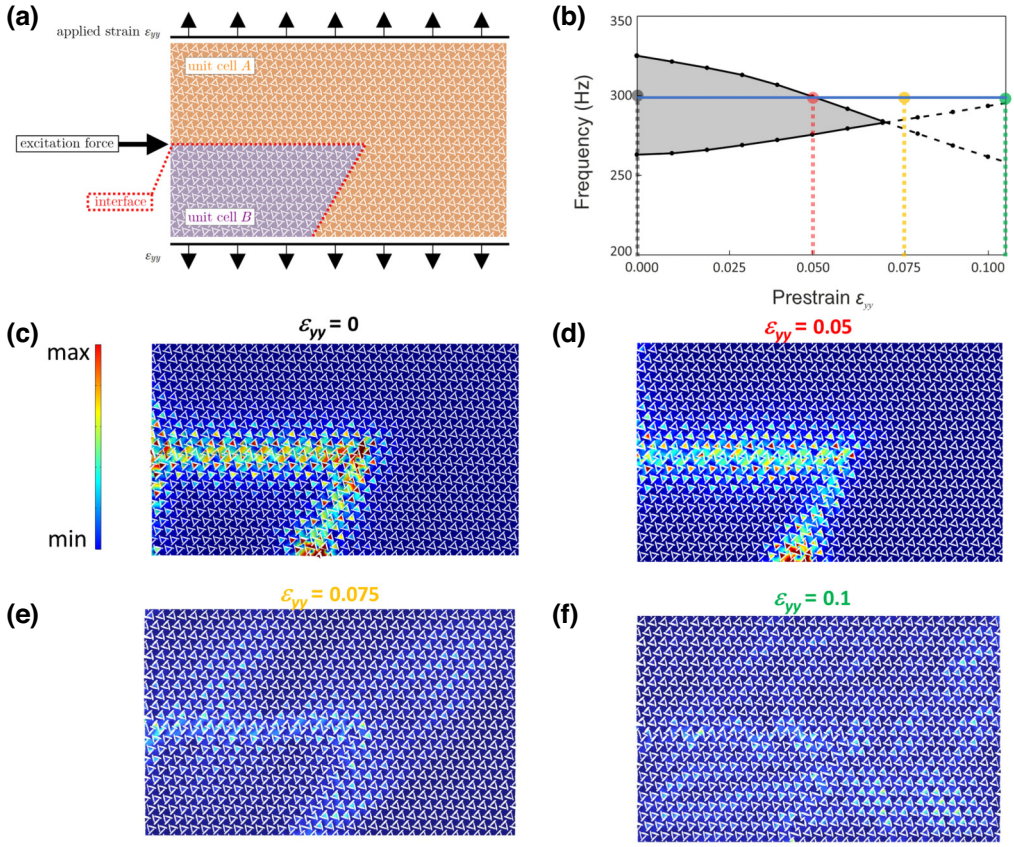

FIG. 8. Tuning of waveguiding by applying an external prestrain ε_{yy}. (a) Schematic of the FEM model for frequency-domain simulations. (b) Detail of the plot in Fig. 7, focusing on the lower topological band gap, highlighting the frequencies and prestrains considered in the simulations. Displacement fields for $f = 300$ Hz and (c) $\varepsilon_{yy} = 0$, (d) $\varepsilon_{yy} = 0.05$, (e) $\varepsilon_{yy} = 0.075$, and (f) $\varepsilon_{yy} = 0.1$, illustrating progressive loss of wave localization for increasing prestrain.

wave localization only along a restricted length, of the order of the distance along which the prestrain is applied, thus allowing wave control in targeted spatial regions of the sample. Very similar results are obtained in other frequency regions, targeting other localized modes discussed previously. While this effect is not optimized in terms of control of transmitted energy through the waveguide, the simulations qualitatively show how it is possible to achieve on-off tunability in waveguiding properties, which can be exploited, e.g., in signal processing applications.

IV. CONCLUSIONS

In conclusion, we have presented a numerical study to demonstrate the possibility of creating reversibly tunable topological metamaterials applying prestrains, exploiting their auxeticity and nonlinearity.

The proposed unit-cell design is simple and requires only the introduction of oriented cuts arranged in a hexagonal pattern within a thin sheet of material. The structure has interesting properties, both quasistatic and dynamic, in that it exhibits auxetic behavior with an extremely negative Poisson's ratio; at the same time, the band structure for both in-plane and out-of-plane modes admits various Dirac cones, which can be exploited for the creation of topological valley modes. The in-plane modes are relatively independent of thickness effects, allowing a 2D treatment of the problem without loss of generality.

The breaking of C_6 symmetry of the unit cells to remove degeneracy is obtained by changing the length of alternate cuts, also allowing parametric design of the desired dispersion properties. We have shown that for the considered structure, this feature occurs only in the presence of cell auxeticity. After C_6-symmetry breaking and construction of macrocells or large lattices with interface regions, we have shown good wave localization at the interface and propagation at sharp edges with negligible backscattering.

Compared to previous designs and conceptual experiments, in this case, the scatter-free waveguiding properties can be manipulated by the simple application of unidirectional quasistatic prestrains of moderate amplitudes (typically below 10%), in which geometrical nonlinearity can be activated. This allows a controlled variation of the unit-cell dispersion properties, with the

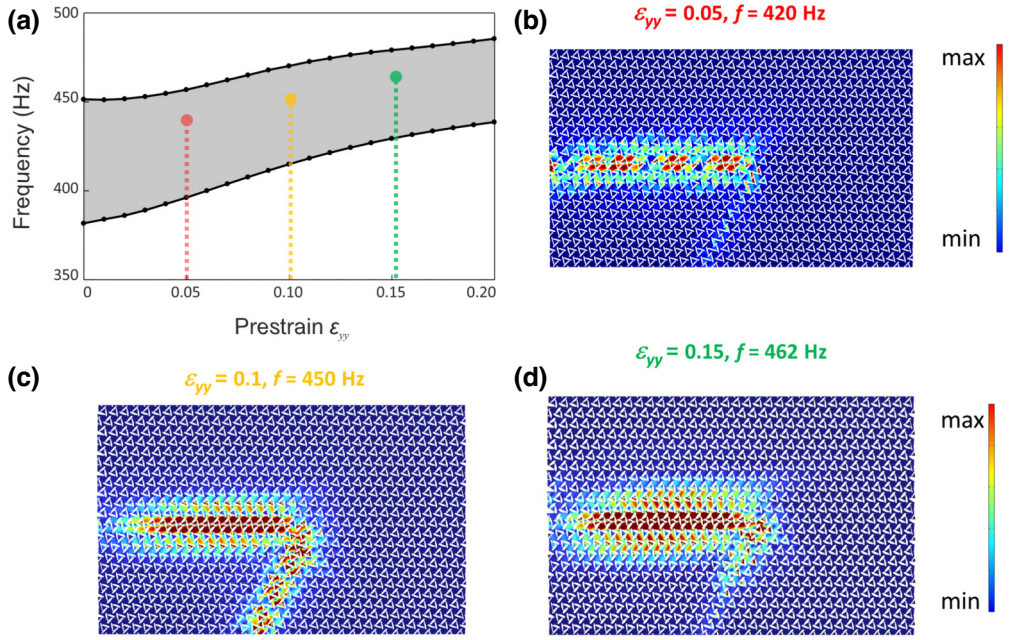

FIG. 9. (a) Detail of the plot in Fig. 7 highlighting the frequencies and prestrains considered in the simulations. Displacement fields showing wave localization at increasing frequencies in the presence of an increasing vertical prestrain ε_{yy}: (b) $f = 440$ Hz for $\varepsilon_{yy} = 0.05$, (c) $f = 450$ Hz for $\varepsilon_{yy} = 0.1$, (d) $f = 462$ Hz for $\varepsilon_{yy} = 0.15$.

removal or shifting of band gaps to higher frequencies, thus enabling the transition from localized waveguiding to nonlocalized propagation. This modification can also be generated in limited portions of the propagation domain, by applying strain that is variable in space or time.

For the proposed design, auxeticity plays a role in this process in various ways: first, it enables large volumetric deformations at relatively low values of stress due to the small bulk modulus, and therefore enables the large deformations necessary to activate nonlinear elastic behavior. In the specific case of the structure considered in

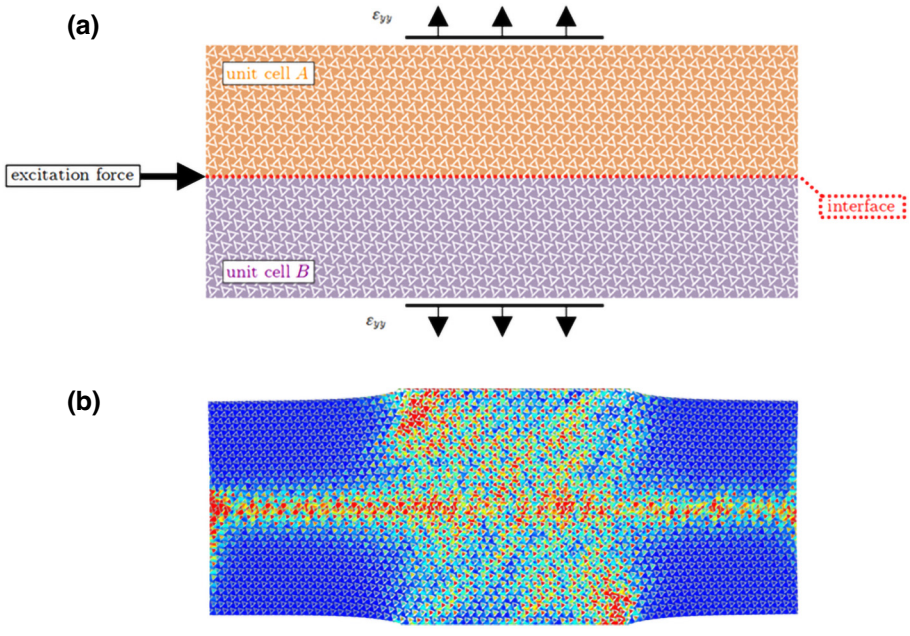

FIG. 10. (a) Schematic of the selected model and loading scenario. (b) Amplitude displacement field for $\varepsilon_{yy} = 0.1$ at 300 Hz. Localized waveguiding is inhibited only in correspondence with the spatial location of the application of prestrain.

this work, auxeticity also enables the appearance of band gaps (see Appendix B) and their variation when prestrain is applied. More specifically, in our design, topological band gaps tend to close for increasing applied prestrain, while nontopological band gaps tend to undergo a frequency shift. The closing of band gaps in the topological case shows a correlation with the decrease of auxeticity due to prestrain (Appendix C). On the other hand, for nontopological band gaps, we observe that the volumetric expansion due to the application of a uniaxial prestrain on an auxetic unit cell leads to a shift of band-gap frequencies.

A future detailed study of how strain states correlate to band-gap modification and topological protection in other auxetic systems will allow these considerations to be potentially generalized.

Given the relative simplicity of the design, these auxetic tunable topological metamaterials should be amenable to fabrication in soft polymeric or elastomeric samples with standard techniques (e.g., moulding and machining), and the required material and geometrical nonlinearity could be generated at relatively small applied prestrain, allowing for an experimental realization of proof-of-concept experiments, and further extending the possibilities in the fast-growing field of tunable metamaterials.

ACKNOWLEDGMENTS

The authors are grateful to Professor Massimiliano Fraldi for useful discussions on Appendix A. M. Mor., V.F.D.P., M. Min., N.M.P., A.S.G., and F.B. are supported by the European Commission H2020 FET Open "Boheme" Grant No. 863179. G.C. and M.B.'s work has been performed under the auspices of GNFM-INDAM; their work has been supported by the European Union's Horizon 2020 RISE MSCA EffectFact Grant No. 101008140. F.B. and N.M.P. are supported by the «AMPHYBIA» project – funded by the Ministero dell'Università e della Ricerca – within the PRIN 2022 program (D.D.104 - 02/02/2022).

APPENDIX A: ISOFREQUENCY CONTOURS

Here, we report the isofrequency contours for the dispersion surfaces of the C_6-symmetric structure shown in Fig. 2(a). The contours have been computed at the low frequencies $f = 10$, 20 Hz and are reported in Figs. 11(a) and 11(b) for the first and second dispersion surfaces, respectively. The "circular" contours indicate the isotropy of the effective behavior. The same result was obtained in Ref. [22] for the hierarchical microstructure but stemming from the too restricting assumption of orthotropy for the considered model.

APPENDIX B: INFLUENCE OF AUXETICITY ON DISPERSION

Here, we present the results of a parametric analysis, where the effective Poisson's ratio of the C_6-symmetric unit cell in Fig. 1(b) is varied by changing the ratio a/l between the cut length and the hexagonal cell size, keeping the angle θ fixed and equal to $\theta = \pi/4$.

The dependence of the macroscopic Poisson's ratio ν_{eff} on the ratio a/l was determined for different values of θ in Ref. [75]. The outcomes for the case $\theta = \pi/4$ are reported in Fig. 12(a). It can be seen that ν_{eff} monotonically decreases as the ratio a/l is increased, varying from positive-to-negative values. In particular, for $a/l = 0.6$ $\nu_{\text{eff}} > 0$ (nonauxetic), while for $a/l = 1.0$ $\nu_{\text{eff}} < 0$ (auxetic).

In Fig. 12(b) we present the dispersion diagrams for the case $a/l = 0.6$, which corresponds to a positive value

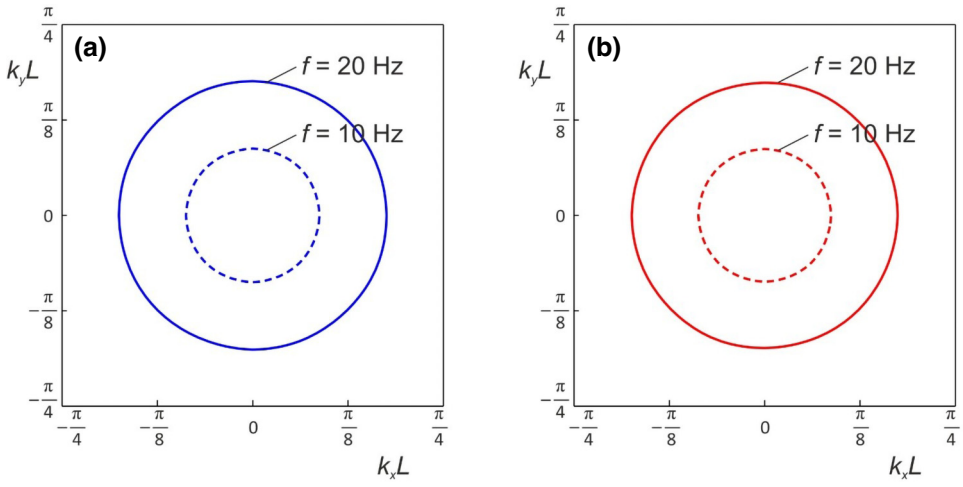

FIG. 11. Isofrequency contours for the (a) first and (b) second dispersion surface of the C_6-symmetric unit cell, computed at two different values of the frequency (i.e., $f = 10$, 20 Hz).

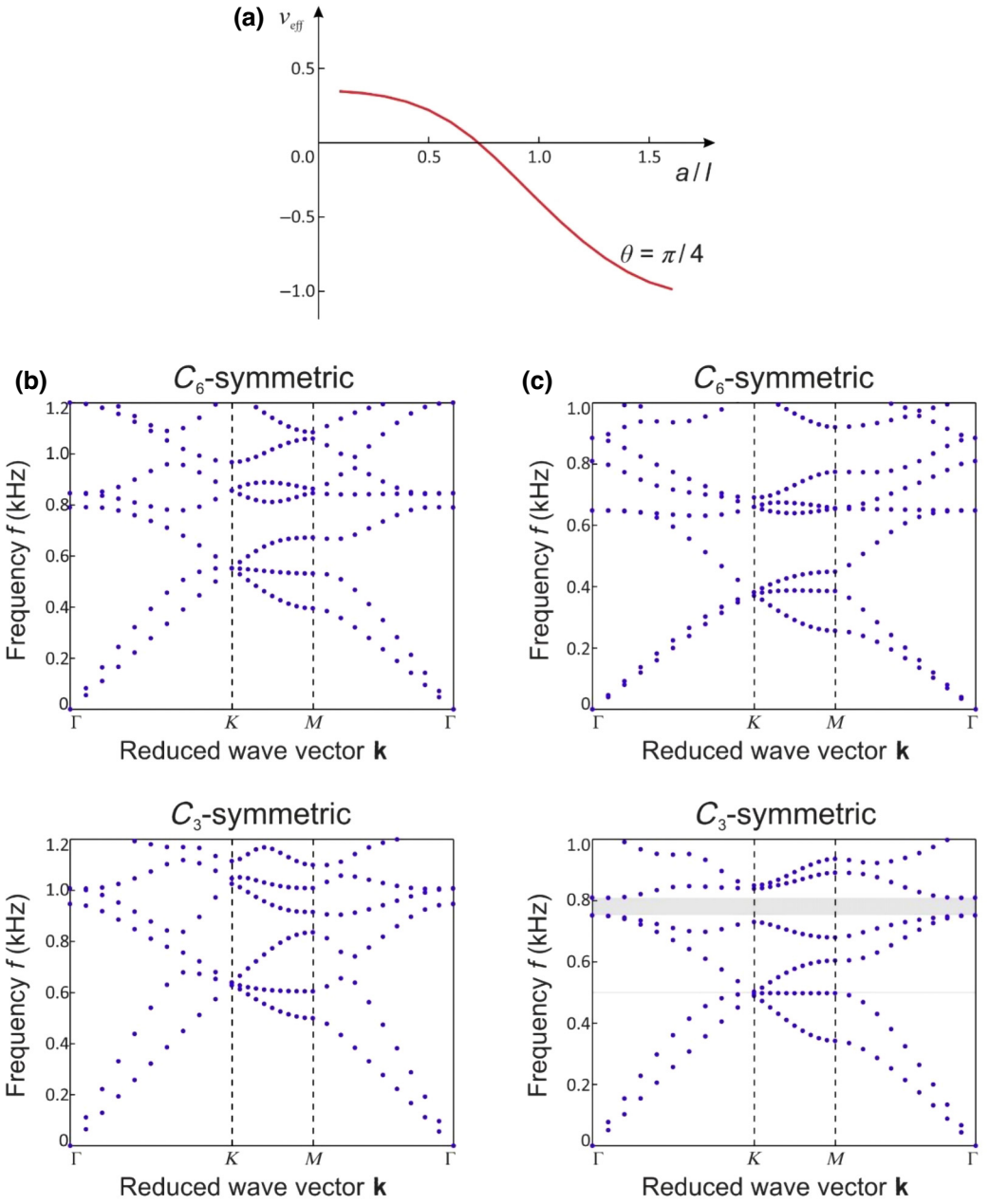

FIG. 12. (a) Effective Poisson's ratio ν_{eff} of the C_6-symmetric unit cell in Fig. 1(b) as a function of the ratio a/l for $\theta = \pi/4$ (data extrapolated from Ref. [75]). Dispersion diagrams for the C_6-symmetric (top insets) and C_3-symmetric (bottom insets) unit cell for (b) $a/l = 0.6$ ($\nu_{\text{eff}} > 0$) and (c) $a/l = 1.0$ ($\nu_{\text{eff}} < 0$).

of the low-frequency effective Poisson's ratio, for the C_6-symmetric unit cell (top figure) and for the C_3-symmetric unit cell (bottom figure) where the cut length reduction is $l' = 2.5$ mm as in Sec. II A. From the figure, it is apparent that the perturbation of the cut lengths does not lead to the opening of a band gap in the proximity of either the lower or upper broken Dirac cone. Consequently, topological wave propagation cannot take place in this situation, where $\nu_{\text{eff}} > 0$.

In Fig. 12(c) we show the band diagrams when the ratio $a/l = 1.0$, for which $\nu_{\text{eff}} < 0$. In this scenario, when the cut lengths are varied, a thin band gap appears in the neighborhood of the lower Dirac cone and another one of consistent width is opened at the upper Dirac cone. Accordingly, topological states can be obtained in this auxetic case.

From the above and further simulations (whose results are not reported here for brevity), we have observed that

the possibility of creating topologically protected waves in the considered medium is closely related to its auxeticity.

APPENDIX C: EVALUATION OF EFFECTIVE POISSON'S RATIO WITH INCREASING PRESTRAIN

In this Appendix, the aim is to investigate if the system remains auxetic after prestrain is applied. For this purpose, we consider a finite structure [see Fig. 13(a)], consisting of 10×15 C_6-symmetric cells, subjected to imposed vertical displacements at the bottom and top boundaries [represented by arrows in Fig. 13(a)]. In order to prevent rigid-body motion, the central point of the structure is constrained. The magnitude of imposed displacement is increased gradually; at each step, the effective Poisson's ratio is calculated as

$$\nu_{xy}^{\text{eff}} = -\frac{(u_B - u_A)/(x_B - x_A)}{(v_D - v_C)/(y_D - y_C)}, \tag{C1}$$

where u and v are the displacement components along the reference coordinate axes x and y. The points A, B, C, and D are indicated in Fig. 13(a).

The values of the effective Poisson's ratio ν_{xy}^{eff} for increasing values of prestrain ε_{yy} are shown in Fig. 13(b). It is apparent that ν_{xy}^{eff} changes slightly in the range of prestrain considered; in addition, the system does not lose its strong auxeticity even if it is subjected to large deformation.

In Figs. 13(c) and 13(d), the color maps of the displacement components u and v, respectively, are presented. The fields are not affected substantially by the boundary conditions. Furthermore, the deformed shapes in Figs. 13(c) and 13(d) are clear evidence that the system is highly auxetic.

Similar computations are performed for a finite system made of C_3-symmetric cells. The results are reported in Fig. 14. In this case, the effective Poisson's ratio increases (i.e., its absolute value decreases) more significantly with the applied prestrain than the model with C_6-symmetric unit cells [see inset (b)]. However, in the range of prestrains considered, the system remains auxetic.

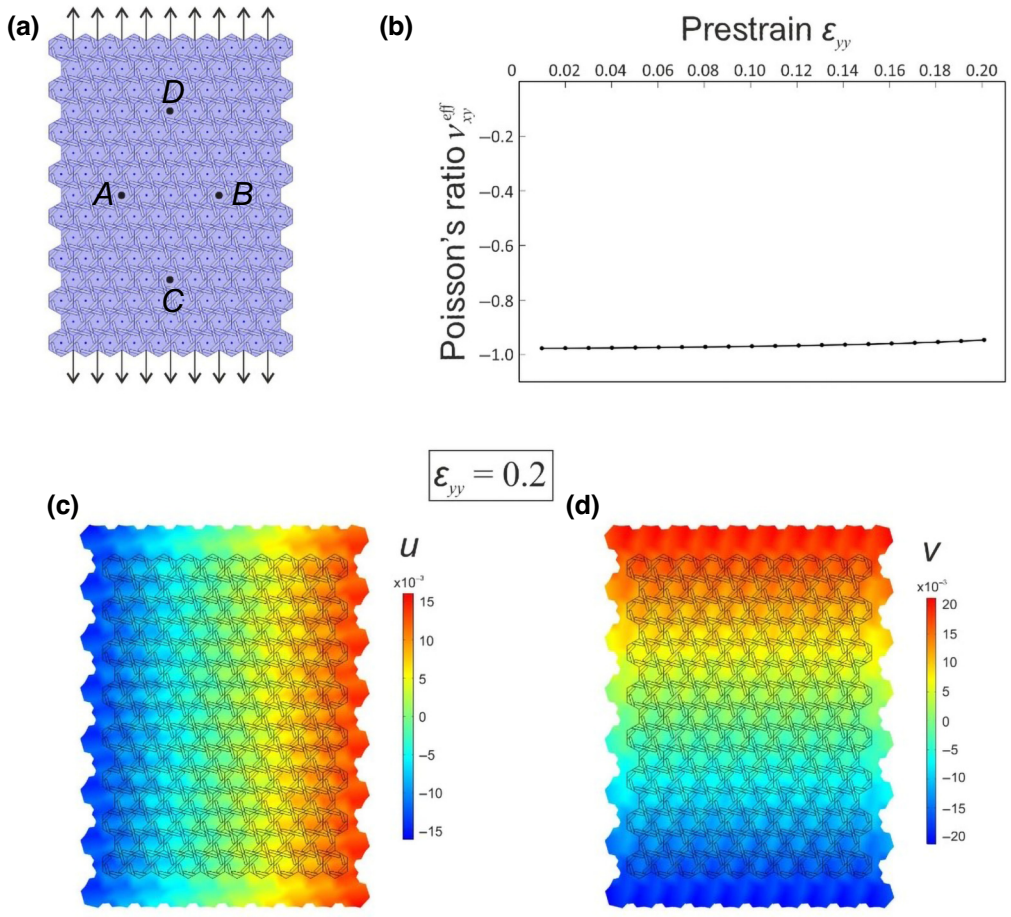

FIG. 13. (a) Finite model, made of 10×15 C_6-symmetric cells and subjected to imposed displacements at the top and bottom boundaries; (b) effective Poisson's ratio ν_{xy}^{eff} versus the imposed engineering strain ε_{yy}; (c),(d) displacement field components u and v, represented in color scale on the deformed configuration at $\varepsilon_{yy} = 0.2$.

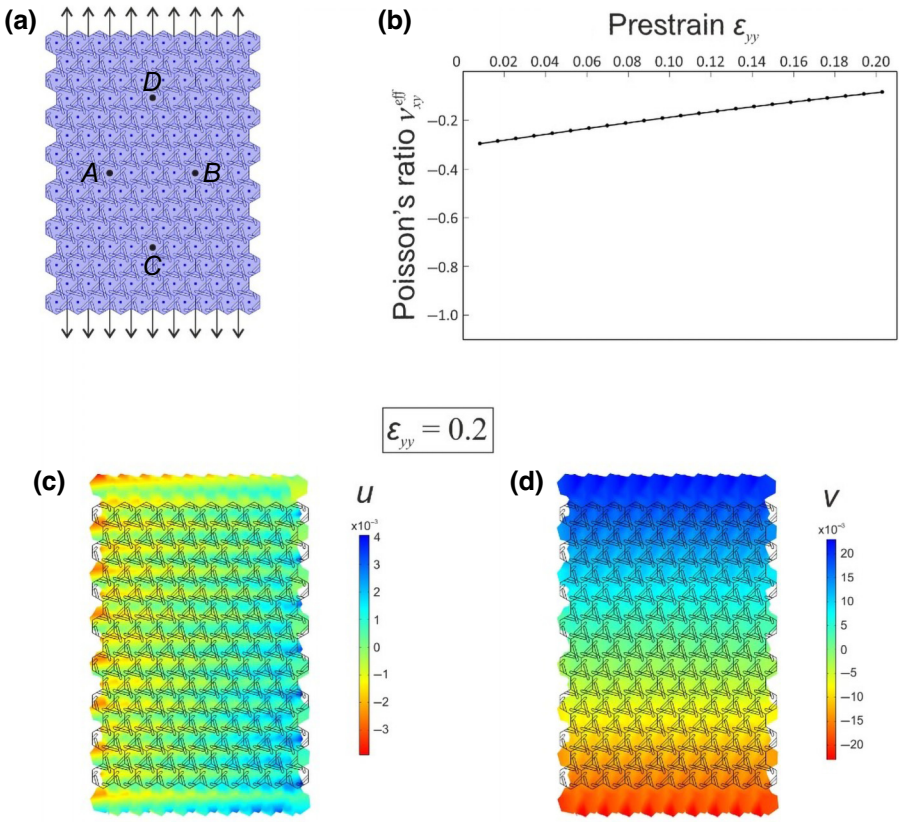

FIG. 14. (a) Finite model, made of 10×15 C_3-symmetric cells and subjected to imposed displacements at the top and bottom boundaries; (b) effective Poisson's ratio ν_{xy}^{eff} versus the imposed engineering strain ε_{yy}; (c),(d) displacement field components u and v, represented in color scale on the deformed configuration at $\varepsilon_{yy} = 0.2$.

From the color map in Fig. 14(c), we observe that the field representing the displacement component u is not symmetric with respect to a vertical axis passing through the center of the model; this is due to the fact that the cells are not C_6 symmetric. The deformed shapes in Figs. 14(c) and 14(d) show that there is a relatively small elongation along the transverse direction, since the effective Poisson's ratio is close to -0.1 for the value of prestrain considered.

APPENDIX D: 3D DISPERSION ANALYSIS AND VALIDATION OF 2D PLANE STRESS RESULTS

In this Appendix, the dispersion properties of hexagonal unit cells are presented considering computations performed using solid FE models (hexahedral elements, characteristic length of 0.25 mm, thus not assuming plane stress behavior) for both C_6-symmetric and C_3-symmetric unit cells (see Fig. 1). These relations are obtained by enforcing periodic Bloch-Floquet boundary conditions on the edges of the unit cell and scanning the contour of the corresponding irreducible Brillouin zone. The same geometrical parameters presented in Sec. II are considered, except for the values of thickness, which range from $h = 0.5$ mm to $h = 2.0$ mm, with increasing steps of 0.5 mm. For each case, a polarization metric in terms of displacement components, given by

$$p = \int_V |u_z|^2 \mathrm{d}V \Big/ \int_V (|u_x|^2 + |u_y|^2 + |u_z|^2)\mathrm{d}V, \qquad \text{(D1)}$$

is computed, which yields a value of 1 (0) for purely out-of-plane (in-plane) wave modes.

Figure 15(a) shows that an increase in the thickness of the unit cell greatly influences the out-of-plane modes ($p \approx 1$), while the in-plane modes ($p \approx 0$) remain practically unchanged. Also, in-plane and out-of-plane modes are fully decoupled due to the symmetry of the unit cell along the out-of-plane axis. The band diagrams corresponding to $h = 1.0$ and $h = 1.5$ mm are omitted for the sake of brevity.

The negligible influence of the unit-cell thickness on the in-plane modes in the dispersion diagrams suggests that a two-dimensional plane stress model is sufficient to capture the representative dynamics of the system associated with in-plane modes. This is shown in Fig. 15(b), where the previously computed dispersion relations using a plane stress assumption [see Sec. II, red hollow circles in Fig. 15(b)]

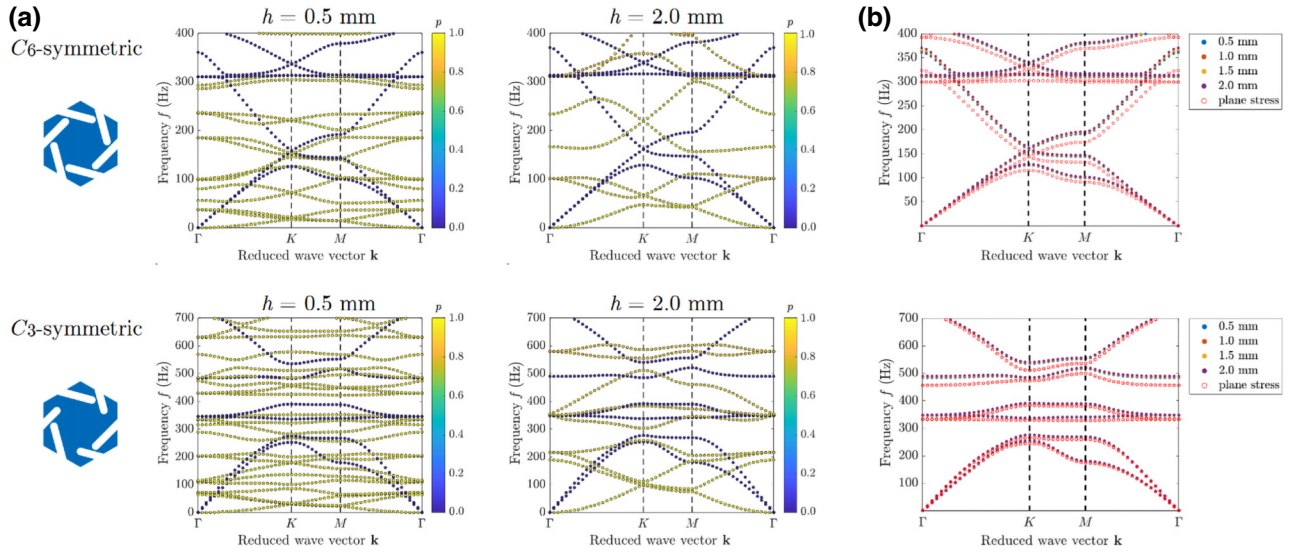

FIG. 15. Band diagrams computed for the (a) solid models of the unit cells with increasing values of thickness h for the C_6-symmetric (top row) and C_3-symmetric (bottom row) unit cells. Color scales refer to polarization values (0 for in-plane, 1 for out-of-plane wave modes). The negligible influence of thickness on in-plane modes suggests the use of a plane stress model as a reasonable approximation, which is confirmed by (b) the comparison between the band diagram of solid models (filled circles) and a plane stress model (red hollow circles).

are indicated as the limit case for solids [filled circles in Fig. 15(b)] with decreasing values of thickness.

[1] R. H. Baughman, Auxetic materials: Avoiding the shrink, Nature **425**, 667 (2003).

[2] R. Lakes, Foam structures with a negative Poisson's ratio, Science **235**, 1038 (1987).

[3] K. K. Saxena, R. Das, and E. P. Calius, Three decades of auxetics research – materials with negative Poisson's ratio: A review, Adv. Eng. Mater. **18**, 1847 (2016).

[4] L. Cabras and M. Brun, A class of auxetic three-dimensional lattices, J. Mech. Phys. Solids **91**, 56 (2016).

[5] P. Mardling, A. Alderson, N. Jordan-Mahy, and C. L. Le Maitre, The use of auxetic materials in tissue engineering, Biomater. Sci. **8**, 2074 (2020).

[6] H. M. A. Kolken, K. Lietaert, T. van der Sloten, B. Pouran, A. Meynen, G. Van Loock, H. Weinans, L. Scheys, and A. A. Zadpoor, Mechanical performance of auxetic meta-biomaterials, J. Mech. Behav. Biomed. Mater. **104**, 103658 (2020).

[7] J. I. Lipton, R. MacCurdy, Z. Manchester, L. Chin, D. Cellucci, and D. Rus, Handedness in shearing auxetics creates rigid and compliant structures, Science **360**, 632 (2018).

[8] K. Chen, S. Fang, Q. Gao, D. Zou, J. Cao, and W. H. Liao, Enhancing power output of piezoelectric energy harvesting by gradient auxetic structures, Appl. Phys. Lett. **120**, 103901 (2022).

[9] K. Chen, Q. Gao, S. Fang, D. Zou, Z. Yang, and W. H. Liao, An auxetic nonlinear piezoelectric energy harvester for enhancing efficiency and bandwidth, Appl. Energy **298**, 117274 (2021).

[10] G. J. Chaplain, J. M. De Ponti, G. Aguzzi, A. Colombi, and R. V. Craster, Topological rainbow trapping for elastic energy harvesting in graded Su-Schrieffer-Heeger systems, Phys. Rev. Appl. **14**, 054035 (2020).

[11] Q. Li, Y. Kuang, and M. Zhu, Auxetic piezoelectric energy harvesters for increased electric power output, AIP Adv. **7**, 015104 (2017).

[12] O. Duncan, T. Shepherd, C. Moroney, L. Foster, P. D. Venkatraman, K. Winwood, T. Allen, and A. Alderson, Review of auxetic materials for sports applications: Expanding options in comfort and protection, Appl. Sci. **8**, 941 (2018).

[13] S. C. Han, D. S. Kang, and K. Kang, Two nature-mimicking auxetic materials with potential for high energy absorption, Mater. Today **26**, 30 (2019).

[14] X. Ren, R. Das, P. Tran, T. D. Ngo, and Y. M. Xie, Auxetic metamaterials and structures: A review, Smart Mater. Struct. **27**, 023001 (2018).

[15] M. Kadic, T. Bückmann, R. Schittny, and M. Wegener, Metamaterials beyond electromagnetism, Rep. Prog. Phys. **76**, 126501 (2013).

[16] T. Li, F. Liu, and L. Wang, Enhancing indentation and impact resistance in auxetic composite materials, Composites, Part B **198**, 108229 (2020).

[17] X. chun Zhang, C. chao An, Z. feng Shen, H. xiang Wu, W. gang Yang, and J. pan Bai, Dynamic crushing responses of bio-inspired Re-entrant auxetic honeycombs under in-plane impact loading, Mater. Today Commun. **23**, 100918 (2020).

[18] L. Francesconi, A. Baldi, X. Liang, F. Aymerich, and M. Taylor, Variable Poisson's ratio materials for globally stable static and dynamic compression resistance, Extreme Mech. Lett. **26**, 1 (2019).

[19] L. Francesconi, A. Baldi, G. Dominguez, and M. Taylor, An investigation of the enhanced fatigue performance of low-porosity auxetic metamaterials, Exp. Mech. **60**, 93 (2020).

[20] H. M. A. Kolken, A. F. Garcia, A. Du Plessis, C. Rans, M. J. Mirzaali, and A. A. Zadpoor, Fatigue performance of auxetic meta-biomaterials, Acta Biomater. **126**, 511 (2021).

[21] R. Gatt, L. Mizzi, J. I. Azzopardi, K. M. Azzopardi, D. Attard, A. Casha, J. Briffa, and J. N. Grima, Hierarchical auxetic mechanical metamaterials, Sci. Rep. **5**, 8395 (2015).

[22] M. Morvaridi, G. Carta, F. Bosia, A. S. Gliozzi, N. M. Pugno, D. Misseroni, and M. Brun, Hierarchical auxetic and isotropic porous medium with extremely negative Poisson's ratio, Extreme Mech. Lett. **48**, 101405 (2021).

[23] E. Baravelli and M. Ruzzene, Internally resonating lattices for bandgap generation and low-frequency vibration control, J. Sound Vib. **332**, 6562 (2013).

[24] S. Krödel, T. Delpero, A. Bergamini, P. Ermanni, and D. M. Kochmann, 3D auxetic microlattices with independently controllable acoustic band gaps and quasi-static elastic moduli, Eng. Mater. **16**, 357 (2014).

[25] L. D'Alessandro, V. Zega, R. Ardito, and A. Corigliano, 3D auxetic single material periodic structure with ultra-wide tunable bandgap, Sci. Rep. **8**, 2262 (2018).

[26] G. U. Patil, A. B. Shedge, and K. H. Matlack, 3D auxetic lattice materials for anomalous elastic wave polarization, Appl. Phys. Lett. **115**, 091902 (2019).

[27] D. Shin, Y. Urzhumov, D. Lim, K. Kim, and D. R. Smith, A versatile smart transformation optics device with auxetic elasto-electromagnetic metamaterials, Sci. Rep. **4**, 4084 (2014).

[28] S. Barik, A. Karasahin, C. Flower, T. Cai, H. Miyake, W. DeGottardi, M. Hafezi, and E. Waks, A topological quantum optics interface, Science **359**, 666 (2018).

[29] M. I. Shalaev, S. Desnavi, W. Walasik, and N. M. Litchinitser, Reconfigurable topological photonic crystal, New J. Phys. **20**, 023040 (2018).

[30] S. Mittal, J. Fan, S. Faez, A. Migdall, J. M. Taylor, and M. Hafezi, Topologically robust transport of photons in a synthetic gauge field, Phys. Rev. Lett. **113**, 087403 (2014).

[31] J. Noh, W. A. Benalcazar, S. Huang, M. J. Collins, K. P. Chen, T. L. Hughes, and M. C. Rechtsman, Topological protection of photonic mid-gap defect modes, Nat. Photonics **12**, 408 (2018).

[32] M. L. N. Chen, L. J. Jiang, Z. Lan, and W. E. I. Sha, Pseudospin-polarized topological line defects in dielectric photonic crystals, IEEE Trans. Antennas Propag. **68**, 609 (2020).

[33] M. Z. Hasan and C. L. Kane, Colloquium: Topological insulators, Rev. Mod. Phys. **82**, 3045 (2010).

[34] X. L. Qi and S. C. Zhang, Topological insulators and superconductors, Rev. Mod. Phys. **83**, 1057 (2011).

[35] L. Lu, J. D. Joannopoulos, and M. Soljačić, Topological photonics, Nat. Photonics **8**, 821 (2014).

[36] S. D. Huber, Topological mechanics, Nat. Phys. **12**, 621 (2016).

[37] H. Huang, J. Chen, and S. Huo, Recent advances in topological elastic metamaterials, J. Phys.: Condens. Matter **33**, 503002 (2021).

[38] E. Prodan and C. Prodan, Topological phonon modes and their role in dynamic instability of microtubules, Phys. Rev. Lett. **103**, 248101 (2009).

[39] L. M. Nash, D. Kleckner, A. Read, V. Vitelli, A. M. Turner, and W. T. M. Irvine, Topological mechanics of gyroscopic metamaterials, Proc. Natl. Acad. Sci. U. S. A. **112**, 14495 (2015).

[40] R. Fleury, A. B. Khanikaev, and A. Alù, Floquet topological insulators for sound, Nat. Commun. **7**, 11744 (2016).

[41] C. He, X. Ni, H. Ge, X. C. Sun, Y. Bin Chen, M. H. Lu, X. P. Liu, and Y. F. Chen, Acoustic topological insulator and robust one-way sound transport, Nat. Phys. **12**, 1124 (2016).

[42] M. Miniaci, R. K. Pal, B. Morvan, and M. Ruzzene, Experimental observation of topologically protected helical edge modes in patterned elastic plates, Phys. Rev. X **8**, 031074 (2018).

[43] J. Lu, C. Qiu, L. Ye, X. Fan, M. Ke, F. Zhang, and Z. Liu, Observation of topological valley transport of sound in sonic crystals, Nat. Phys. **13**, 369 (2017).

[44] R. Fleury, D. L. Sounas, C. F. Sieck, M. R. Haberman, and A. Alù, Sound isolation and giant linear nonreciprocity in a compact acoustic circulator, Science **343**, 516 (2014).

[45] A. Souslov, B. C. van Zuiden, D. Bartolo, and V. Vitelli, Topological sound in active-liquid metamaterials, Nat. Phys. **13**, 1091 (2017).

[46] C. Brendel, V. Peano, O. J. Painter, and F. Marquardt, Pseudomagnetic fields for sound at the nanoscale, Proc. Natl. Acad. Sci. U. S. A. **114**, E3390 (2017).

[47] S. H. Mousavi, A. B. Khanikaev, and Z. Wang, Topologically protected elastic waves in phononic Metamaterials, Nat. Commun. **6**, 8682 (2015).

[48] R. K. Pal and M. Ruzzene, Edge waves in plates with resonators: An elastic analogue of the quantum valley Hall effect, New J. Phys. **19**, 025001 (2017).

[49] R. K. Pal, M. Schaeffer, and M. Ruzzene, Helical edge states and topological phase transitions in phononic systems using Bi-layered lattices, J. Appl. Phys. **119**, 084305 (2016).

[50] S. G. Haslinger, S. Frecentese, and G. Carta, Localized waves in elastic plates with perturbed honeycomb arrays of constraints, Philos. Trans. R. Soc., A **380**, 20210404 (2022).

[51] M. Miniaci and R. K. Pal, Design of topological elastic waveguides, J. Appl. Phys. **130**, 141101 (2021).

[52] Y. Jin, D. Torrent, and B. Djafari-Rouhani, Robustness of conventional and topologically protected edge states in phononic crystal plates, Phys. Rev. B **98**, 054307 (2018).

[53] K. Sun, A. Souslov, X. Mao, and T. C. Lubensky, Surface phonons, elastic response, and conformal invariance in twisted kagome lattices, Proc. Natl. Acad. Sci. U. S. A. **109**, 12369 (2012).

[54] C. L. Kane and T. C. Lubensky, Topological boundary modes in isostatic lattices, Nat. Phys. **10**, 39 (2013).

[55] J. Paulose, B. G. G. Chen, and V. Vitelli, Topological modes bound to dislocations in mechanical metamaterials, Nat. Phys. **11**, 153 (2015).

[56] M. Miniaci, R. K. Pal, R. Manna, and M. Ruzzene, Valley-based splitting of topologically protected helical waves in elastic plates, Phys. Rev. B **100**, 024304 (2019).

[57] Z. Tian, C. Shen, J. Li, E. Reit, H. Bachman, J. E. S. Socolar, S. A. Cummer, and T. Jun Huang, Dispersion tuning and route reconfiguration of acoustic waves in valley topological phononic crystals, Nat. Commun. **11**, 762 (2020).

[58] Y. Chen, X. Liu, and G. Hu, Topological phase transition in mechanical honeycomb lattice, J. Mech. Phys. Solids **122**, 54 (2019).

[59] Y. F. Wang, Y. Z. Wang, B. Wu, W. Chen, and Y. S. Wang, Tunable and active phononic crystals and metamaterials, Appl. Mech. Rev. **72**, 040801 (2020).

[60] N. K. Mohammadi, P. I. Galich, A. O. Krushynska, and S. Rudykh, Soft magnetoactive laminates: Large deformations, transverse elastic waves and band gaps tunability by a magnetic field, J. Appl. Mech., Trans. ASME **86**, 111001 (2019).

[61] A. S. Gliozzi, M. Miniaci, A. Chiappone, A. Bergamini, B. Morin, and E. Descrovi, Tunable photo-responsive elastic metamaterials, Nat. Commun. **11**, 2576 (2020).

[62] J. Hwan Oh, I. Kyu Lee, P. Sik Ma, and Y. Young Kim, Active wave-guiding of piezoelectric phononic crystals, Appl. Phys. Lett. **99**, 083505 (2011).

[63] B. I. Popa and S. A. Cummer, Non-reciprocal and highly nonlinear active acoustic metamaterials, Nat. Commun. **5**, 3398 (2014).

[64] A. Darabi, M. Collet, and M. J. Leamy, Experimental realization of a reconfigurable electroacoustic topological insulator, Proc. Natl. Acad. Sci. U. S. A. **117**, 16138 (2020).

[65] Q. Zhang, Y. Chen, K. Zhang, and G. Hu, programmable elastic valley Hall insulator with tunable interface propagation routes, Extreme Mech. Lett. **28**, 76 (2019).

[66] M. Miniaci, M. Mazzotti, A. Amendola, and F. Fraternali, Effect of prestress on phononic band gaps induced by inertial amplification, Int. J. Solids Struct. **216**, 156 (2021).

[67] M. Mazzotti, I. Bartoli, and M. Miniaci, Modeling Bloch waves in prestressed phononic crystal plates, Front. Mater. **6**, 74 (2019).

[68] M. Gei, A. B. Movchan, and D. Bigoni, Band-gap shift and defect-induced annihilation in prestressed elastic structures, J. Appl. Phys. **105**, 063507 (2009).

[69] T. W. Liu and F. Semperlotti, Tunable acoustic valley-Hall edge states in reconfigurable phononic elastic waveguides, Phys. Rev. Appl. **9**, 014001 (2018).

[70] K. Bertoldi and M. C. Boyce, Mechanically triggered transformations of phononic band gaps in periodic elastomeric structures, Phys. Rev. B **77**, 052105 (2008).

[71] J. R. Raney, N. Nadkarni, C. Daraio, D. M. Kochmann, J. A. Lewis, and K. Bertoldi, Stable propagation of mechanical signals in soft media using stored elastic energy, Proc. Natl. Acad. Sci. U. S. A. **113**, 9722 (2016).

[72] K. Bertoldi, V. Vitelli, J. Christensen, and M. van Hecke, Flexible mechanical metamaterials, Nat. Rev. Mater. **2**, 17066 (2017).

[73] K. E. Evans and A. Alderson, Auxetic materials: Functional materials and structures from lateral thinking!, Adv. Mater. **12**, 617 (2000).

[74] M. Kheybari, C. Daraio, and O. R. Bilal, Tunable auxetic metamaterials for simultaneous attenuation of airborne sound and elastic vibrations in all directions, Appl. Phys. Lett. **121**, 081702 (2022).

[75] G. Carta, M. Brun, and A. Baldi, Design of a porous material with isotropic negative Poisson's ratio, Mech. Mater. **97**, 67 (2016).

[76] A. Baldi, M. Brun, and G. Carta, Three-dimensional auxetic porous medium, Mech. Mater. **164**, 104114 (2022).

[77] A. Auld, *Acoustic Fields and Waves in Solids* (John Wiley and Sons, New York, 1973), Vol. I.

[78] E. N. Peters, in *Mechanical Engineers' Handbook*, edited by M. Kutz (John Wiley & Sons, Inc., Hoboken, New Jersey, 2015).

[79] J. Lu, C. Qiu, S. Xu, Y. Ye, M. Ke, and Z. Liu, Dirac cones in two-dimensional artificial crystals for classical waves, Phys. Rev. B: Condens. Matter Mater. Phys. **89**, 134302 (2014).

[80] X. Xie, H. Li, Y. Peng, X. Zhu, W. Luo, and D. Zhao, Switching between deterministic and accidental dirac degeneracy by rotating scatterers and the multi-channel topological transport of sound, New J. Phys. **21**, 073047 (2019).

[81] S. Li, I. Kim, S. Iwamoto, J. Zang, and J. Yang, Valley anisotropy in elastic metamaterials, Phys. Rev. B **100**, 195102 (2019).

[82] P. Wang, L. Lu, and K. Bertoldi, Topological phononic crystals with one-way elastic edge waves, Phys. Rev. Lett. **115**, 104302 (2015).

[83] M. Pastor, M. Binda, and T. Harčarik, Modal assurance criterion, Procedia Eng. **48**, 543 (2012).

[84] J. Vila, R. K. Pal, and M. Ruzzene, Observation of topological valley modes in an elastic hexagonal lattice, Phys. Rev. B **96**, 134307 (2017).

[85] R. W. Ogden, *Non-Linear Elastic Deformations* (Dover Publications, Inc., Mineola, New York, 1997).

[86] M. M. Attard, Finite strain - isotropic hyperelasticity, Int. J. Solids Struct. **40**, 4353 (2003).